Acoustic emission location in flexocaloric single crystals

Author: Emma Valdés Martín
Facultat de Física, Universitat de Barcelona, Diagonal 645, 08028 Barcelona, Spain.

Advisor: Eduard Vives Santa-Eulalia

Abstract: Single crystals undergoing a strain-induced martensitic transition produce ultrasonic acoustic emission. A CuAlNi elongated sample is bent and unbent at a constant rate to cause the martensitic transformation between a cubic and a monoclinic phase. We have been able to detect and locate the fronts that separate the two phases by using three piezoelectric ultrasonic sensors. Additionally, we have measured the energies of the acoustic emission events and fitted their statistical distribution to a log-normal probability density.

I. INTRODUCTION

In response to climate change, new technologies are constantly being developed to replace current environmentally damaging practices. One promising prospect is to replace vapor compression heat pumps, which commonly use greenhouse gases as refrigerants, with solid-state devices based on caloric materials [1].

Caloric effects consist in the release or absorption of heat caused by an adiabatic temperature change, or an isothermal entropy change, under the influence of an applied field. While many materials display some sort of caloric effect, efficient caloric materials typically undergo first-order transitions. That makes them more interesting from the commercial standpoint, since the caloric effect is intensified by the release or absorption of large amounts of latent heat. Caloric materials are named after the field that drives their transformation: elastocaloric solids display caloric effect under the influence of uniaxial tensile stress, barocaloric solids do the same under applied pressure, magnetocalorics under a magnetic field, and so on [1]. The flexocaloric effect is similar to the elastocaloric effect, but is induced by bending or twisting. Flexocaloric materials exhibit a caloric response under a strain gradient. Devices based on these materials are expected to be easier to implement in industrial applications [2].

Martensitic transformations (MTs) are first-order, diffusionless structural phase transitions. Atoms in a material undergoing a MT rearrange from a high symmetry phase (known as the austenite) to a low symmetry phase (known as the martensite). Typically, the austenite is a cubic phase and the martensite can be either a tetragonal, orthorhombic or monoclinic phase. The transformation involves a shape change of the unit cell with little change in volume. At zero stress, it can be induced by cooling below the martensite start temperature M_s. At room temperature, the transition can be induced by applying uniaxial stress above σ_{trans}. The domains of the martensitic phase can grow in different energetically equivalent orientations that constitute different variants. When inducing the transformation by cooling, all variants grow simultaneously, giving rise to the so-called martensitic microstructure. When the transition is induced by applying external stress, the growing variants are the ones favorable to the local deformation. Many interesting properties of these materials arise from the MT, such as superelasticity, shape memory and high damping [3, 4].

A key aspect of MTs is their dynamics. During a MT, the martensite advances in the solid at the expense of the cubic phase. This process is controlled by nucleation and subsequent growth. Nucleation is the formation of microscopic volumes of martensite within the austenite domain. This new configuration causes a change of free energy that depends on the nucleus's size. Above a critical size, total free energy is minimized with growing nuclei and the propagation of the martensitic phase becomes favorable [4–6]. Phase fronts advance across the solid, propagating in impulsive jumps ('jerks') and displaying avalanche-like motion. Avalanche behavior occurs when the system has many different metastable configurations due to the presence of imperfections in the lattice [6]. Advancing domain walls in a MT produce crackling noise, a type of acoustic emission that is found in many systems at very different size scales, going from crumpling paper to earthquakes. These systems often exhibit fat-tailed (usually power-law) distributions of avalanche energies and avalanche sizes [7].

Acoustic emission (AE) happens when ultrasonic waves propagate in a material as a result of sudden deformation [8]. AE detection is a commonly used technique for tracking and quantifying MT phase front dynamics. It is possible to locate sources of AE (events) using more than one transducer, in a similar way an earthquake's epicenter can be located by triangulation of multiple seismometers' data. AE has successfully been used to locate domain walls in MTs [9]. For d-dimensional location, at least $d+1$ transducers are required. Experimental results of inducing a MT at a constant deformation rate (hard-driven MT) by elongating a CuZnAl sample concluded that fronts do not advance simultaneously but intermittently. It also has been found that most AE happens during the martensite-to-austenite transition. Power-law behavior for the distribution of energy and amplitude in MTs has also been obtained from many AE based experiments [8, 9].

In this work, an elongated CuAlNi sample is bent and

unbent at a constant displacement rate. This induces a MT in the solid. The main goal is to detect and locate AE to track the movement of transition fronts. Getting a better understanding of how fronts propagate can be useful for diverse applications of caloric materials, in which it is crucial to know where latent heat is being released or absorbed. Finally, we will also study the distribution of the AE event energy. The maximum likelihood method [10] will be carried out to confirm the presence of a fat-tailed distribution.

II. EXPERIMENTAL SETUP

A. Sample

The sample used for this experiment is a single-crystal $Cu_{67.7}Al_{26.7}Ni_{5.6}$ (at.%) beam with dimensions 99.15 mm (long) × 5 mm (width) × 1 mm (depth). It transforms from a cubic austenite to a monoclinic martensite. The martensite has 12 equivalent variants to accommodate stress. By differential scanning calorimetry, it has been determined that this sample has $M_s \approx 260$ K. By applying uniaxial stress at room temperature, it has been found that $\sigma_{\text{trans}} \approx 100$ MPa.

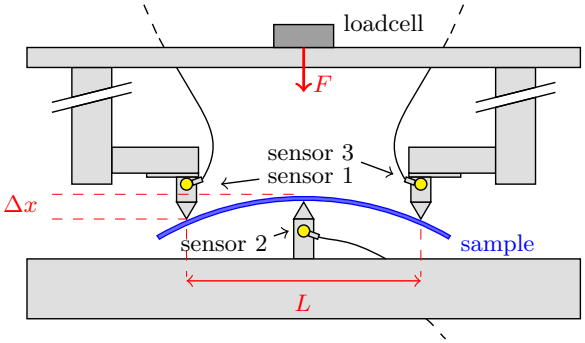

FIG. 1: Sketch of the inverted 3-point flexural test. The two pins above are vertically displaced by the materials testing machine. The applied force F is measured by the loadcell on the upper part of the setup. AE sensors are placed on each pin.

B. Inverted 3-point flexural test

The experiment conducted is an inverted 3-point flexural test of a beam. The beam is placed on the fixture of a testing machine Zwick/Roell Z005. Two pins on the upper surface and one pin on the lower surface bend the beam as shown in Fig. 1. The pins on top are separated a distance $L = (60.00 \pm 0.01)$ mm. This setup is called inverted, since a regular 3-point flexural test has 2 pins below and one pin above. An AE sensor is attached to the outward face of each pin. The surface of the sensors, as well as the spots of the sample that are in contact with a pin, have previously been coated with vaseline to ensure a good ultrasonic contact. The main frame of the machine has a crosshead that performs a controlled vertical motion, and a loadcell converts the total vertical applied force to voltage. In the experiment, the initially unbent beam is bent to a maximum displacement (Δx in Fig. 1) of 25 mm. The testing machine then pauses for 30 s in order to thermalize the sample, and after that it returns to the original unbent state. This is done at a constant rate of 1 mm/min. Such a low rate allows to better separate AE events (groups of hits that allow a successful location).

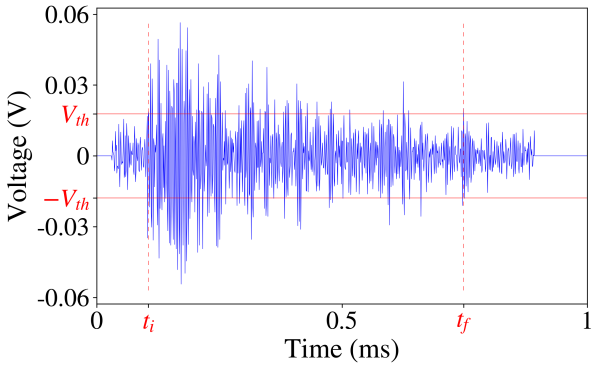

FIG. 2: Signal of a single AE hit with $A = 35$ dB and duration $T = t_f - t_i$.

C. AE detection

The sensors that were used in the experiment are piezoelectric acoustic transducers with an optimal response in the ultrasonic frequency range 200 kHz−1 MHz. Voltages in the sensors were preampified to 60 dB, such that the signal amplitude (in dB) for a peak voltage V_p detected by a sensor is calculated using:

$$A\ (\text{dB}) = 20 \log_{10}(V_{\text{p}}/1\,\mu\text{V}) - 60\,\text{dB}. \qquad (1)$$

The amplified signals are input to a PCI-2 card (Europhysical Acoustics) that allows for the processing of acoustic signals by means of AEwin software. AE data includes the register of hits, their amplitude, energy and duration. A hit is a single AE signal. An AE signal starts being recorded when the voltage crosses a threshold V_{th} for the first time. It ends when it remains below threshold for more than 100 μs. The time difference between the first and last crossing is the duration of the hit. A real example is shown in Fig. 2. The energy of a hit is computed as the integral of the squared voltage divided by the reference resistance over its duration:

$$E = \frac{1}{R}\int_{t_i}^{t_f} V^2 dt. \qquad (2)$$

The reference resistance is $R = 10\,\text{k}\Omega$. The threshold voltage has been set to 25 dB, according to the relation in Eq.(1). Applied force and displacement are transferred as a parametric input from the materials testing machine software to AEwin and exported along the acquired AE data.

III. METHODS

A. Model

The study considers a one-dimensional approach, and location is computed for the longitudinal dimension z. Distances between the sample's surface and each sensor are neglected. This is valid when all three distances are equal. If that applies, the location of the AE source z_0 remains unaffected and the only effect is a time shift for all events. Another approximation being made is that the length of the beam doesn't change as the experiment advances, which is false for the real case of bending. The deformation of the length of the beam is neglected. Lastly, velocity of acoustic waves is taken constant across the sample, neglecting the effect of having two different structural phases in the solid.

B. AE location

The location of AE sources was determined using a Python code. The foundations of the algorithm are sketched in Fig. 3. There are three hits recorded for every

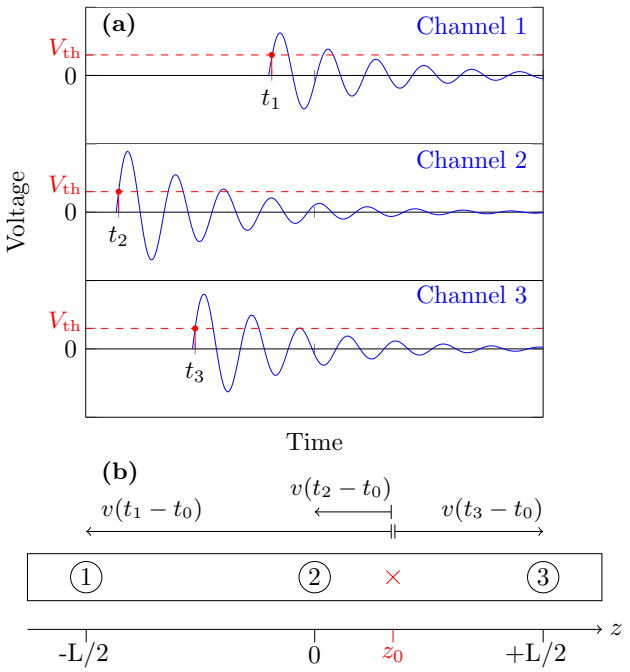

FIG. 3: Basis of AE location. (a) Example of a detected voltage signal on each sensor's channel. **(b)** Schematic of the sample (not to scale). Position of each sensor indicated by circled numbers 1,2,3.

event, since there are three sensors placed across the sample. An event occurs at (t_0, z_0). Since $t_2 < t_3 < t_1$, the order in which the signal has reached each sensor is 231. There are 4 possible sequences. The other three are 123, 213 and 321. Each combination corresponds to an event originated in a different quarter of the sample. The code looks for consecutive hits that satisfy these sequences.

Any event that takes place between two sensors can be located using those two sensors. This means that there are two possible methods available to locate every event: either by using sensors 1 and 3, or by using the two closest sensors to the event. Location of AE cannot be performed outside boundaries $\left[-\frac{L}{2}, \frac{L}{2}\right]$. According to a constant speed model, location for Fig. 3 is computed as follows:

$$\left.\begin{aligned} z_0^{13} &= \frac{1}{2}v(t_1 - t_3), \\ t_0^{13} &= \frac{1}{2}(t_1 + t_3 - t_{max}), \end{aligned}\right\} \tag{3}$$

$$\left.\begin{aligned} z_0^{23} &= \frac{1}{4}L + \frac{1}{2}v(t_2 - t_3), \\ t_0^{23} &= \frac{1}{2}\left(t_2 + t_3 - \frac{1}{2}t_{max}\right), \end{aligned}\right\} \tag{4}$$

where L, t_1, t_2, t_3 are known and $t_{max} \equiv L/v$ is the time it takes for a wave traveling at v ($v > 0$) to cross the distance L in the sample. Superscripts refer to the pair of sensors used for the location. If location is perfect, then $z_0^{13} = z_0^{23}$. This generally is not the case, and the difference serves well as an estimate of the error bar for z_0.

An estimate for velocity v can be computed with the help of Python package `scipy.optimize`. There are a lot of friction-related signals, mainly associated to pins 1 and 3. These show as high-energy signals. Since it is known that they should occur at $z = \pm L/2$, we select the value v that places most friction signals in these positions. We obtain $v = 1030\,\mathrm{mm/s}$.

Besides t_0 and z_0, event energy E_0 can also be calculated. If E_i, E_j are the energies measured by sensors i, j used in the computation of (t_0^{ij}, z_0^{ij}), source energy for an AE event can be approximated as:

$$E_0^{ij} = \sqrt{E_i E_j}, \qquad ij = \{12, 23, 13\}. \tag{5}$$

This expression assumes a constant attenuation factor across the sample. Since energy in this experiment spans a few decades and is expected to follow a fat-tailed distribution, it is important to characterize the size of events using the logarithm of E_0.

C. Statistical analysis for event energy

The statistical distribution of the event energy has been fitted to a log-normal distribution using the maximum likelihood method. The log-normal probability density is:

$$f(E)dE = \frac{1}{\sqrt{2\pi\sigma^2}E}\exp\left[-\frac{(\ln E - \mu)^2}{2\sigma^2}\right]dE, \tag{6}$$

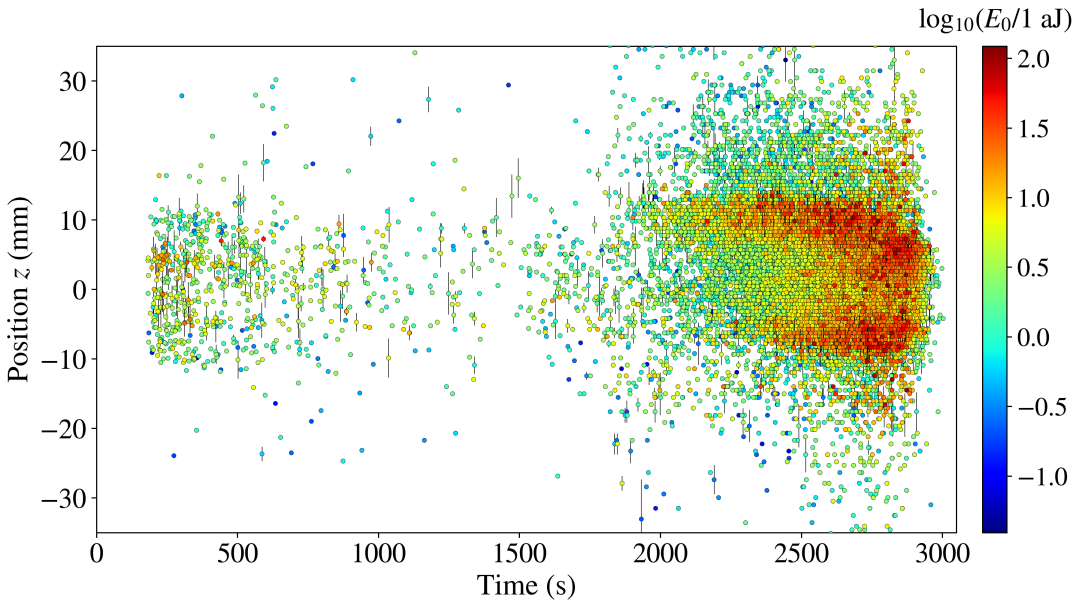

FIG. 4: AE source location of a sample undergoing a MT induced by an inverted 3-point flexural test. Displacement changes at a rate of 1 mm/min. AE shown in the figure has been located using pairs of sensors 12 or 23. Some representative error bars have been included. The color scale represents the size of the events, characterized as $\log_{10}(E_0/1\,\mathrm{aJ})$.

where parameters μ and σ^2 are computed as follows:

$$\mu = \frac{\sum_{i=1}^{n} \ln E_i}{n},\ \sigma^2 = \frac{\sum_{i=1}^{n} \left(\ln E_i - \frac{\sum_{i=1}^{n} \ln E_i}{n}\right)^2}{n}. \quad (7)$$

$\{E_1, \ldots E_n\}$ is the set of recorded event energies [10].

IV. RESULTS

Fig. 4 shows a scatter graph revealing the position of AE events as a function of time. The color of every point corresponds to the source energy of the event, as indicated in the bar on the right. Error bars have been determined as explained in methods.

Fig. 5 shows the corresponding evolution of the pin displacement Δx (Fig. 5a), the vertical force (Fig. 5b) and a summary of the acoustic activity (Fig. 5c). In this last plot we represent two histograms computed on intervals of 10 s; in blue the number of AE hits, and in red the number of AE events.

The first comment is that in the first and last ~ 200 s of the experiment, there is almost no AE, despite the increasing applied force. Both time intervals correspond to the elastic deformation of the austenite phase that does not show any AE event.

There is a clear asymmetry between the bending stage (first 1500 s) and the unbending stage (last 1500 s). The number of events in the direct transition (austenite to martensite) is 30 times less than in the reverse transition (martensite to austenite). This asymmetry has already been found in the literature [11] when studying the same MT induced by temperature changes.

By looking at Fig. 4, it is difficult to evaluate where AE

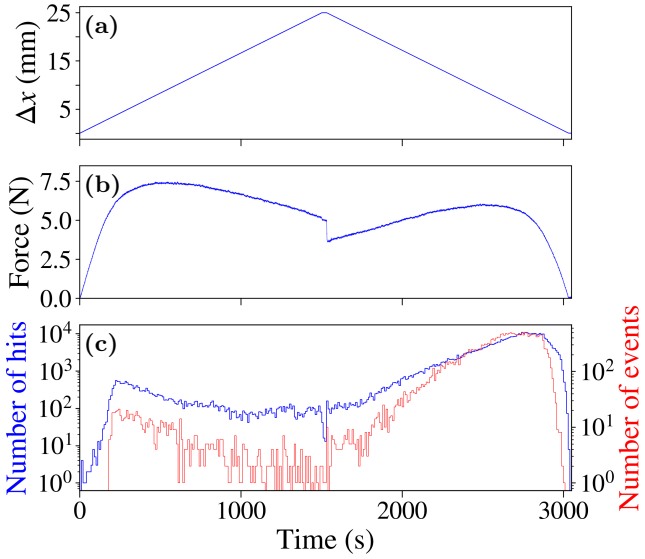

FIG. 5: Evolution of the 3-point flexural test. **(a)** Vertical displacement of the moving pins, at rate 1 mm/min. **(b)** Vertical force applied to bend the beam. **(c)** AE activity throughout the experiment. A total of 485722 hits were detected and 24944 events were located.

concentrates during bending. During unbending, however, it is clear that two fronts with AE signals above 10 aJ start at $z = \pm 10$ mm and move towards the center of the sample, where they merge. Note that after bending, both ends of the beam were still in the cubic phase since they had not been stressed. Two fronts separate the martensitic phase in the center from the austenite in

the sides. When unbending, both fronts move towards the center until the whole sample is transformed back to austenite.

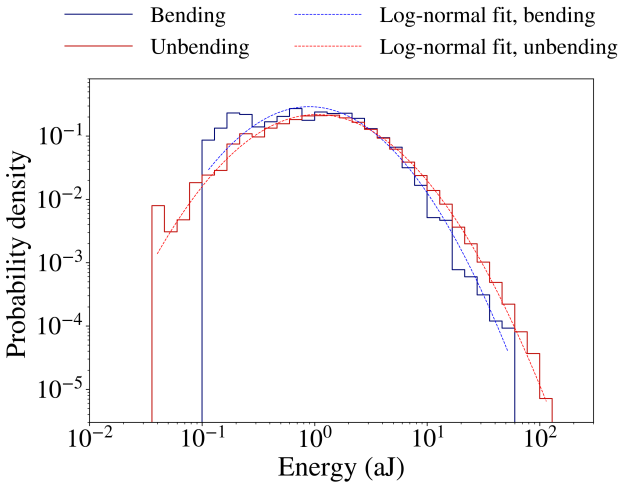

FIG. 6: Event energy distribution and log-normal fit for bending (blue) and unbending (red).

At the end of the reverse transition, high-energy events are sparsely distributed along the entire sample. These might correspond to small monoclinic domains that were untransformed and suddenly transform back to cubic when stress is low enough.

Finally, we would like to point out that after the reversal point (change of the driving velocity around 1500 s) the force exhibits a drop of more than 1 N. This hysteresis can be understood as an elastic relaxation of the martensitic domains. Note that in this interval there is almost no AE.

Fig. 6 shows histograms corresponding to the statistical distribution of all the event energies recorded during bending (blue) and unbending (red). Event energies during both stages can be well fitted with log-normal distributions with the following parameters:

	μ	σ^2	$\exp\mu$ (aJ)	$\exp\sigma$ (aJ)
Bending	0.819	0.927	2.268	2.619
Unbending	1.104	1.054	3.017	2.792

TABLE I: Parameters of the log-normal fit calculated with the maximum likelihood method.

In future studies we will deepen in the reasons behind the fact that these distributions are not power-law (as expected for thermally induced MTs) but log-normal.

V. CONCLUSIONS

In this work, we have successfully located AE events in a CuAlNi single crystal undergoing a MT in a bending/unbending experiment. This has allowed us to observe the trajectory of the transformation fronts.

- The proposed AE location technique is a good tool to monitor the dynamics of the martensitic-austenitic phase fronts. The technique allows us to locate AE events with a resolution of ±3 mm.
- The MT starts only when strain increases beyond the elastic regime of the austenite (cubic) phase.
- The acoustic activity during unbending surpasses by a factor of 30 the activity during bending.
- AE event energies in bending/unbending experiments are statistically distributed according to a log-normal probability density.

Acknowledgments

First, I would like to thank my advisor E. Vives for his guidance throughout the entire process, and for the opportunity to learn about such an interesting subject.

I would also like to thank my peers and family for all their help and support.

[1] Moya, X. and Mathur, N. D.. "Caloric materials for cooling and heating". Science **370**: 797-803 (2020).
[2] Porta, M., Castán, T., Saxena, A. and Planes, A.. "Flexocaloric effect near a ferroelastic transition". Phys. Rev. B **104**: 094108 (2021).
[3] Wayman, C. M.. "Solid-State Phase Transformations". Annu. Rev. Mater. Sci. **1**: 185-218 (1971).
[4] R. Abbaschian, L. Abbaschian and R. Reed-Hill, *Physical Metallurgy Principles*, (Cengage Learning, Stamford 2009, 4th. ed.).
[5] S. Sridhar, and H. Sohn, *Fundamentals of Metallurgy*, 270-349 (Woodhead Publishing, Sawston 2005, 1st. ed.).
[6] Nataf, G. F. and Salje, E. K. H.. "Avalanches in ferroelectric, ferroelastic and coelastic materials: phase transition, domain switching and propagation". Ferroelectrics **569**: 82-107 (2020).
[7] Sethna, J. P., Dahmen, K. A. and Myers, C. R.. "Crackling noise". Nature **410**: 242-250 (2001).
[8] Blaysat, B., Balandraud, X., Grédiac, M., Vives, E., Barrera, N. and Zanzotto, G.. "Concurrent tracking of strain and noise bursts at ferroelastic phase fronts". Commun. Mater. **1**: 3 (2020).
[9] Vives, E., Soto-Parra, D., Mañosa, L., Romero, R. and Planes, A.. "Imaging the dynamics of martensitic transitions using acoustic emission". Phys. Rev. B **84**: 060101 (2011).
[10] Ginos, B. F.. "Parameter estimation for the lognormal distribution". Thesis and Dissertations. 1928 (2009).
[11] Planes, A. and Vives, E.. "Avalanche criticality in thermal-driven martensitic transitions: the asymmetry of the forward and reverse transitions in shape-memory materials". J. Phys. Condens. Matter. **29**: 334001 (2017).